Int. J. Electrochem. Sci., 11 **(2016)** 5021 – 5034, doi: 10.20964/2016.06.46

International Journal of
ELECTROCHEMICAL
SCIENCE
www.electrochemsci.org

Stress Corrosion Cracking Behavior of TP95S tube Steel in an Acidic Gas Field Environment

Yong Li[1], *Zhiyong Liu*[1,*], *Le Ke*[1], *Luyao Huang*[1], *Cuiwei Du*[1], *Xiaogang Li*[1]

[1] Corrosion and Protection Center, Key Laboratory for Corrosion and Protection (MOE), University of Science and Technology Beijing, Beijing 100083, China
[*]E-mail: liuzhiyong7804@126.com

Received: 9 September 2015 / *Accepted:* 30 March 2016 / *Published:* 4 May 2016

Stress corrosion cracking (SCC) of TP95S tube steel was investigated through electrochemical measurement and electrochemical hydrogen charging, as well as immersion corrosion and slow strain rate tensile tests. The SCC mechanism of TP95S steel in the acidic gas field solution is mixed controlled by anodic dissolution (AD) and hydrogen embrittlement (HE). The SCC susceptibility of TP95S is lower at 100 °C than that at 60 °C because of abated HE. When the tensile stress reaches more than 70% of the yield strength of TP95S tube steel, TP95S exhibits SCC. Thus, stress applied to TP95S tube steel in service should be lower than 70% and 50% of the yield strength at 100 °C and 60 °C, respectively. Furthermore, tensile stress decreases the service life of TP95S tube steel in the acidic gas field.

Keywords: TP95S tube steel; acidic gas field; stress corrosion cracking

1. INTRODUCTION

Stress corrosion cracking (SCC) of tube steel in acidic gas field solutions significantly affects oil and gas industries in terms of economical perspective [1, 2].

Several studies have demonstrated the mechanism underlying the influence of temperature on corrosion in H2S solutions [3–7]. In an H2S environment, FeSx film is formed on the oxide film surface [8]. H2S and other acidic media can react with the metal substrate by passing through the FeSx layer and the inner oxide film; this mechanism generates hydrogen, which enters into the metal, accelerates anodic dissolution, and enhances SCC susceptibility [9, 10]. With increasing temperature, the corrosion products become denser, which leads to enhanced protective effect on the substrate [11, 12]. But temperature increases the activity of ion and metal surface and promotes ion diffusion through the membrane [13, 14], which leads to high rate of chemical reaction.

The increases of the production hydrogen will enhance SCC susceptibility, however, the increasing of temperature will decreases hydrogen content in the metal, which leads to reduce SCC susceptibility. So it is need to study and analysis the effect of temperature to SCC susceptibility. And the SCC behavior and mechanism in high temperature and high pressure is different from that at room temperature and atmosphere pressure. As a new kind of sulfur-resistant tube steel, TP95S is widely used in oil and gas fields. Nevertheless, a few studies have investigated the stress corrosion mechanism and the relationship between SCC susceptibility and corrosion temperature of TP95S in oil and gas.

In this work, the SCC behavior and mechanism of TP95S tube steel in an acidic gas field environment were investigated through electrochemical measurement and electrochemical hydrogen charging, as well as immersion corrosion and slow strain rate tensile (SSRT) tests.

2. EXPERIMENTAL

Test specimens were cut from a TP95S plate, whose chemical composition and mechanical properties are shown in Tables 1 and 2, respectively. The work electrodes for electrochemical tests were embedded in epoxy resin, with a working area of 1.0 cm^2. Electrodes preparation was carefully controlled to avoid grooving and bubbling at the epoxy/steel interface. The working surface was subsequently polished using 1500 grit emery papers and cleaned with distilled water and ethanol.

Specimens for immersion, constant load tensile, and SSRT tests were prepared according to GB T15970 specifications; the specimens were elongated in the rolling direction, with specimen sizes based on the requirements shown in Fig. 1. The test section was polished with 1500 grit emery paper, cleaned with distilled water and ethanol, dried with cold air, and weighed to a precision of 10 mg. The work area was also measured. The remaining specimens were covered by heat-resistant silicone rubber.

Table 1. Chemical composition of TP95S steel (mass fraction/%).

Element	C	Mn	S	P	Cr	Ni
Content	0.31	1.12	0.005	0.008	0.085	0.009

Table 2. Mechanical properties of TP95S steel.

Yield strength (MPa)	Fracture strength (MPa)	Elongation (%)	Reduction of area (%)
763	837	24.1	58.6

Corrosion solution was prepared with chemical reagents according to the chemical composition of well liquid obtained from a gas field in the southwest of China (Table 3). The concentration of H_2S was adjusted to 300 mg/L by adding N_2S to the corrosion solution. The pH of the solution was also adjusted with HCl to simulate the acid gas field environment (mass fraction 5%).

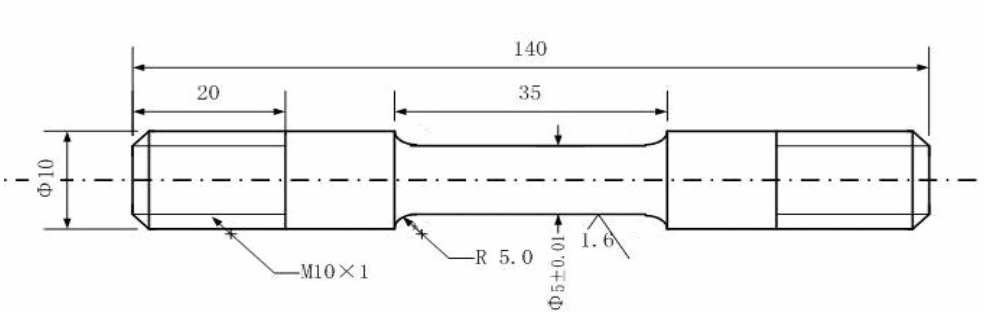

Figure 1. Sample for immersion, constant load tensile, and SSRT tests.

Table 3. Chemical composition of the simulated solution (mg/L).

NaCl	KCl	$CaCl_2$	$MgCl_2$	pH
4710	780	33850	33600	5.0

Prior to each test, solutions were purged with high-purity nitrogen gas for 12 h to remove oxygen. The deoxygenated solution was placed in the autoclave and rapidly sealed after specimen installation. The partial pressures of CO_2 and of N_2 are 0.6 and 9.4 MPa in all the tests. The testing system was set to the required temperatures.

Potentiodynamic polarization curves and electrochemical impedance measurements were conducted on an APR multi-channel electrochemical workstation in an electrochemical three-electrode cell, with the TP95S steel electrode used as working electrode, a saturated calomel electrode as reference electrode, and a platinum plate as counter electrode. The potential sweep rate was set as 0.5 mV/s, and experiment temperatures were 25 °C, 60 °C, and 100 °C.

About 5 mm-thick TP95S steel was used for electrochemical hydrogen electrochemical hydrogen charging. Prior to electrochemical hydrogen charging, the surfaces of all the specimens ware mechanically polished. An arsenic aqueous solution (0.25 g of 0.5 mol, H2SO4/1 L of H2O) was used as the electrolyte in the tests. The samples were charged at 30 °C, 40 °C, 50 °C, and 90 °C, with similar electrochemical hydrogen charging duration (24 h) and current density (50 mA/cm2). After electrochemical hydrogen charging, the samples were placed in liquid paraffin, and the amount of hydrogen released was measured.

Specimens for immersion corrosion were divided into no-stress and tensile-stress specimens, with an applied stress 50% of the yield strength. Experimental conditions are shown in Table 4. In each test, six constant load specimens were tested: two for the calculation of corrosion rate, and four for SSRT and constant load tensile tests. After corrosion for a stipulated time without stirring, the specimens were removed from the autoclave and rinsed with deionized water. The two specimens for corrosion rate test were descaled in a solution with 500 mL of HCl, 500 mL of H_2O, and 5 g of $C_6H_{12}N_4$. The specimens were then rinsed with water and absolute alcohol, dried in air, and weighed to determine the final mass. The average corrosion rate was expressed as the uniform rate of thickness loss per unit time in millimeters per annum ($mm \cdot a^{-1}$) and calculated according to Eq. (1):

$$R_W = \frac{\Delta g \times 8.76 \times 10^5}{ATp} \quad (1)$$

where R is the average corrosion rate, mm/a^{-1}; ∆g is the mass loss, g; A is the initial exposed surface area of the specimens, mm^2; T is the exposure time, h; and ρ is the density of metal, g·cm^{-3}.

The specimens for SSRT and constant load tensile tests were not descaled. The loads for the constant load tensile tests were 50%, 70%, 80%, and 90% of the yield strength, respectively. The strain rate for the SSRT tests was set as 5×10^{-7} S^{-1}.

The microstructures of the steel samples were observed through optical microscopy. The morphologies of the side face and fracture surface of the specimens after SSRT and constant load tensile tests were determined through scanning electron microscopy (SEM).

The remaining life of TP95S in the environment was predicted based on mass loss. The security factor of the average corrosion rate was 1.3, and the initial thickness of the TP96S tube was 12.5 mm. Instability without stress is defined as leakage caused by corrosion thinning, whereas instability with tensile stress is described as SCC or mechanical faults that occur when the actual stress exceeds the yield strength because of corrosive thinning.

Table 4. Experimental conditions for immersion corrosion tests.

Group	P_{CO2}/MPa	P_{N2}/MPa	Temperature/ °C	Immersion time/h
Group 1	0.6	9.4	60	120
Group 2	0.6	9.4	100	120, 240, 360, 720

3. RESULTS AND DISCUSSION

3.1. Microstructure of TP95S tube steel

Figure 2. Microstructure of TP95S tube steel.

Fig. 2 shows the microstructure of the TP95S steel specimen, which contains a ferrite matrix. The phases of the steel are relatively small and uniform and have no inclusions.

3.2. Influence of solution temperature on the electrochemical behavior of TP95S tube steel

Electrochemical polarization curves were assessed to determine the influence of solution temperature on the electrochemical behavior of TP95S tube steel. Fig. 3 displays the polarization curves of the TP95S steel specimen at different temperatures of the corrosion solution. The corrosion potential Ecorr at the temperature of 25 °C shows higher value closed to -600 mV (SCE). And the value of Ecorr at high temperature (60 °C) is -700 mV (SCE). But the value at higher temperature (100 °C) is not higher than that at the temperature with the value about -650 mV. Sosa and Garcia have pointed that sulphides is semiconductor, which has passivation property and limits diffusion of ions [15]. In this way, the results suggest that the increase of the corrosion potential as the temperature increasing from 60 °C to 100 °C is caused by the denser of corrosion products. Furthermore, it is similar to the research of Eliyan [11] and Kairi [12].

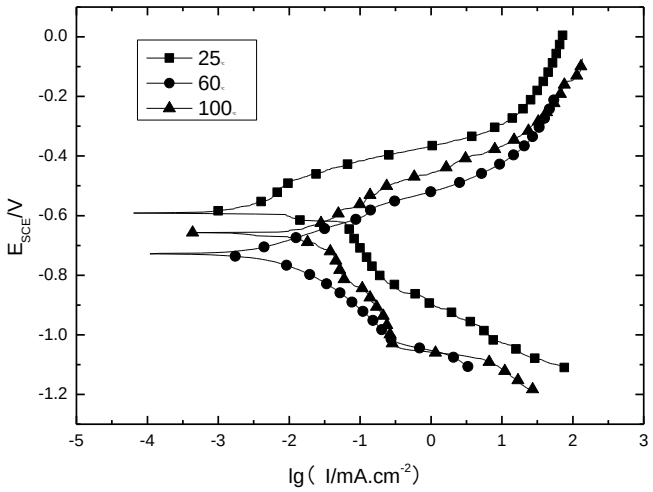

Figure 3. Polarization curves of TP95S steel at different temperatures of corrosion solution.

The kinetic parameters obtained from the data in Fig. 3 are shown in Table 5 according the methodology in [16]. Corrosion rate increases as the corrosion temperature increases from 25 °C to 60 °C and 100 °C, which could be due to low charge-transfer resistance. The temperature generally has significant impact on the kinetic parameters of the reaction [17]. The increase of temperature enhances the activity of ion, which leads to the augment of corrosion current [13, 14].

Table 5. Kinetic parameters obtained from the data in Fig. 3

Temperature（°C）	E_{corr} mV vs. V_{SCE}	I_{corr}Acm^{-2}	b_a mV/dec	b_C mV/dec
25	-596	3.16×10^{-6}	161	-347
60	-702	4.5×10^{-6}	141	-146
100	-655	1.54×10^{-5}	122	-195

Fig. 4 depicts the Nyquist plots for the TP95S steel specimen at different temperatures of the corrosion solution. The specimen exhibits the lowest impedance semicircle at a solution temperature of 100 °C. An increase in Zim and Zre (Nyuist) with the increasing of temperature is observed. This finding indicates poor corrosion resistance, and that higher solution temperatures can accelerate corrosion. It is the same with the result of electrochemical polarization curve.

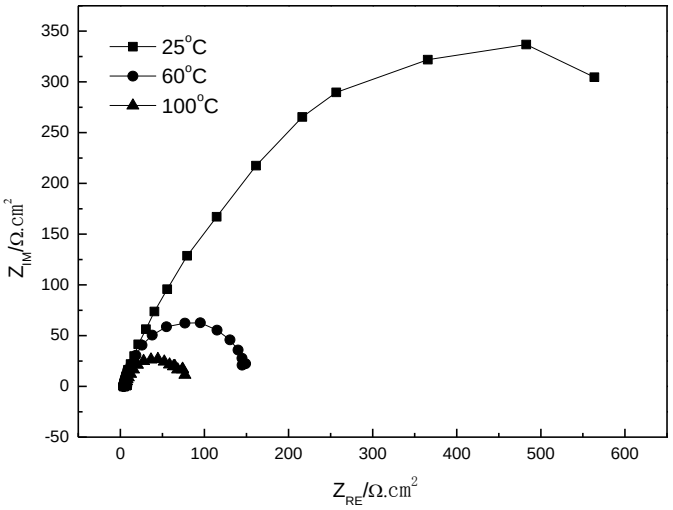

Figure 4. Nyquist plots for TP95S steel at different temperatures of corrosion solution**.**

EIS data were fitted using the ZSimpWin software to explain the corrosion process. The equivalent circuit of the TP95S steel specimen in the corrosion solution was obtained by a non-linear regression fitting [18]. Fig. 5 shows the equivalent circuit model used for fitting EIS diagrams in Fig. 4, which is similar to the study in [19]. In the model, Rs is the resistence of solution, Q1 is the capacitance of double-layer, R1 represents the charge-transfer resistance of oxidation reaction, and the parallel arrangement Q2-R2 describes the diffusion of iron ions through the film of corrosion products [15]. EIS simulated with Re fitted well with the simulated measurement, which indicates the suitability of the equivalent circuit.

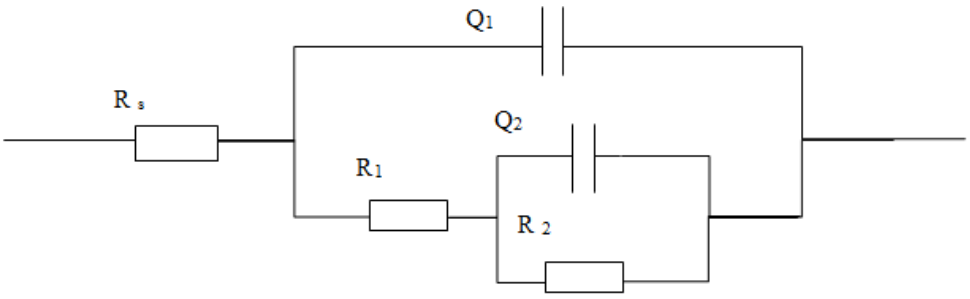

Figure 5. Equivalent circuit of TP95S steel in corrosion solution.

. Table 6 displays the EIS results of the TP95S steel specimen at different temperatures of the corrosion solution in the equivalent circuit. The values of R1 and R2 (1.60 Ω cm2 and 153 Ω cm2)at the temperature of 60°C are lower than the values of R1 and R2 (5.89 Ω cm2 and 445 Ω cm2) at the lower

temperature (25°C). And the value of R2 decreases to 16.4 Ω cm2 at higher temperature. However, the value of R1 increases to 68.0 Ω cm2 at the highest temperature of 100°C, which is higher than that at the temperature of 25°C and 60°C . R1 and R2 represent the charge-transfer resistance of oxidation reaction and the diffusion resistance of iron ions, respectively. According to the results above and the study in [11-14,20], we can conclude that temperature enhances electrochemical reaction rate. And the film of corrosion products becomes denser and compact at higher temperature (from 60 °C to 100 °C) in an acidic gas field environment, which inhibit the corrosion.

Table 6. EIS analysis results of TP95S steel at different temperatures of corrosion solution.

Temp （°C）	R s (Ω cm2)	Q1 （Ssecncm-2）	n 1	R 1 (Ω cm2)	Q 2 （Ssecncm-2）	n 2	R 2 (Ω cm2)
25	5.099	2.36×10-3	0.961	5.89	1.24×10-3	0.924	445
60	3.878	0.719×10-3	1	1.60	1.97×10-3	0.801	153
100	5.53	6.44×10-3	0.844	68.0	301×10-3	1	16.4

In solutions containing H2S, the gas dissolves in water and gradually ionizes [21]:

$H2S \leftrightarrow HS- + H+$

$HS- \leftrightarrow S2- + H+$

The cathodic and anodic reactions of TP95S tube steel in the deaerated acidic solution are reduction of hydrogen irons and oxidation of iron, respectively:

$H+ + e \rightarrow H$

$Fe \rightarrow Fe2+ + 2e$

In solutions with low pH, Fe2+ concentration rapidly increases. A layer of the corrosion product of FeSx is formed on the steel surface, as indicated by the presence of S2− ions in the solution; this product reduces steel corrosion.

$Fe2+ + S2- \rightarrow FeSx$

However, iron diffusion in the film is strongly enhanced with increasing temperature, thus increasing corrosion rate.

3.3 Electrochemical hydrogen charging

Fig. 6 depicts the relationship between the amount of hydrogen released and electrochemical hydrogen charging temperature. The amount of hydrogen absorbed by TP95S steel during corrosion is one-tenth lower at the electrochemical hydrogen charging temperature of 90 °C than that at 30 °C. The steel in the H2S medium can produce hydrogen, which enters into the metal, thereby accelerating anodic dissolution and enhancing SCC. As such, SCC susceptibility at 100 °C is lower than that at 60 °C.

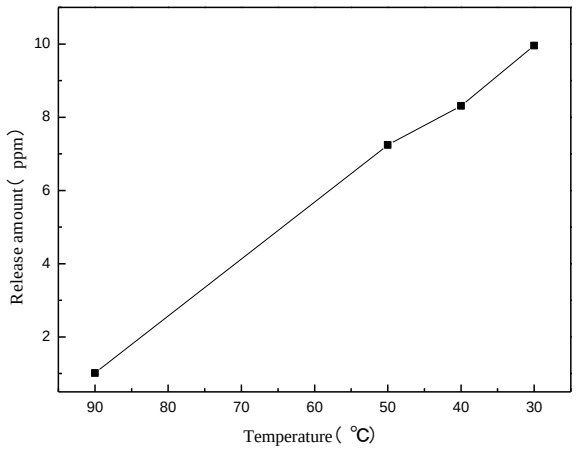

Figure 6. Relationship between hydrogen release and electrochemical hydrogen charging temperature.

3.4 Stress–strain curve

Fig. 7 shows the stress–strain curves of no-stress specimens under different constant loads after immersion in the solution for 720 h at 100 °C. The applied load considerably influences the tensile property. When the tensile stress increases from 50% to 70% of the yield strength, the strength and elongation rate are gradually reduced.

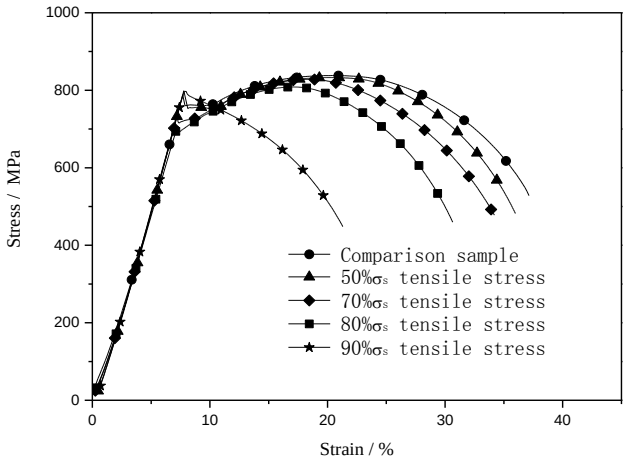

Figure 7. Stress–strain curves of no-stress specimens under different constant loads after soaking in simulated liquid for 720 h at 100 °C.

When the tensile stress increases to 90% of the yield strength, the elongation rate significantly decreases up to the rate wherein SCC sensitivity is not apparent. However, when tensile stress is lower than 80% of the tensile strength, SCC sensitivity considerably decreases. Hence, the threshold value of SCC ranges from 80% to 90% of the yield strength.

Fig. 8 shows the stress–strain curves of the tensile specimens after immersion in simulated liquid for different durations at varied temperatures. TP95S tube steel exhibits good mechanical

properties at 100 °C, whereas the elongation rate of TP95S decreases drastically at 60 °C. Low temperatures can thus enhance SCC susceptibility.

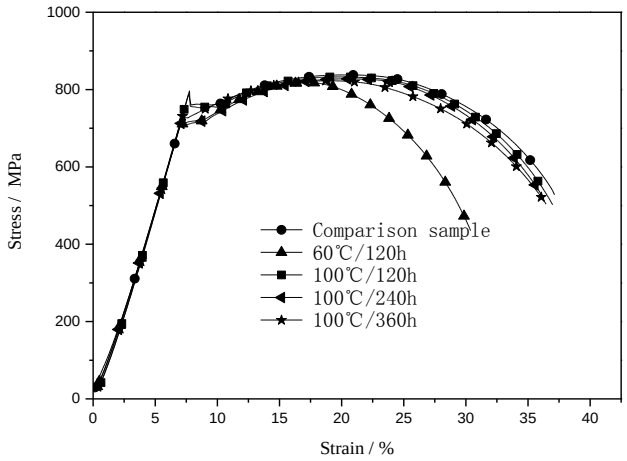

Figure 8. Stress–strain curves of tensile specimens after soaking in simulated liquid for different durations at different temperatures.

Reduction-in-area (I_δ) and elongation-loss rate (I_η) are calculated to investigate the susceptibility of the steel at different constant loads in the solution, and the results are shown in Fig. 9.

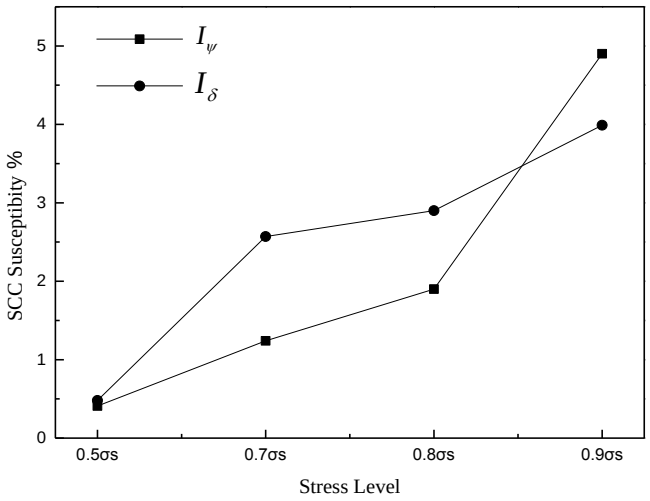

Figure 9. Applied load dependence of SCC susceptibility.

The two rates are defined as

$$I_\delta = \left(1 - \frac{\delta_E}{\delta_o}\right) \times 100\% \quad (2)$$

$$I_\eta = \left(1 - \frac{\Psi_E}{\Psi_o}\right) \times 100\% \quad (3)$$

where δ_E and Ψ_E are tensile reduction-in-area and elongation of steel at applied constant load, respectively; and δ_o and Ψ_o are reduction-in-area and elongation of steel measured in air, respectively.

As shown in Fig. 9, I_δ and I_η increase with increasing applied constant load. As I_δ and I_η are ductility-loss parameters, a positive shift of the applied load increases the SCC susceptibility of the steel. SCC susceptibility gradually increases when the applied load is less than 80% of the yield strength and significantly increases when the applied stress increases from 80% to 90% of the yield strength. Hence, the threshold value of SCC ranges from 80% to 90% of the yield strength.

3.5. Surface morphologies of steel after the tests

Fig. 10 shows the SEM images of the fracture surfaces of the steel specimens after SSRT and immersion in the solution for 120 h at different temperatures. Despite the occurrence of necking, no obvious secondary cracks exist on the side faces. The fracture surfaces exhibits ductility with extensively distributed simples on the surface at 100 °C. By contrast, the fracture surfaces demonstrate brittleness, with river-bed shaped crack orientation at 60 °C. These findings indicate that SCC susceptibility is lower at 100 °C than that at 60 °C.

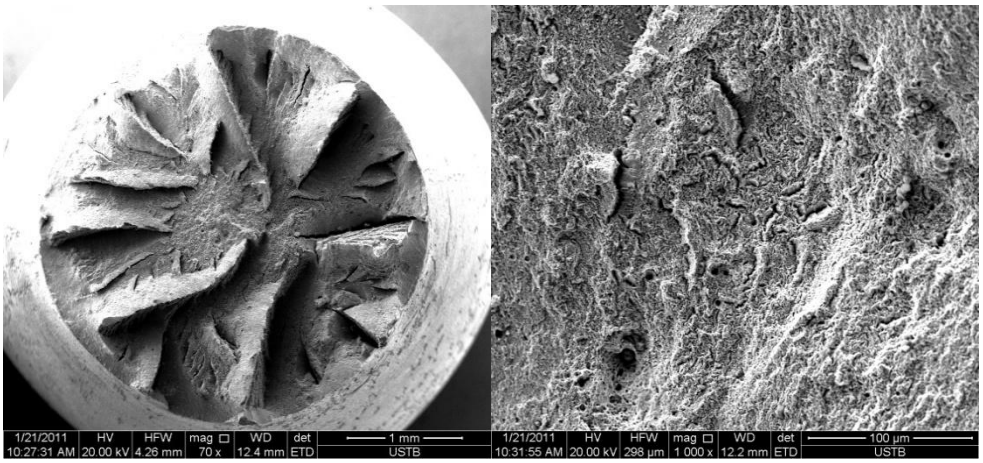

(a) 60 °C

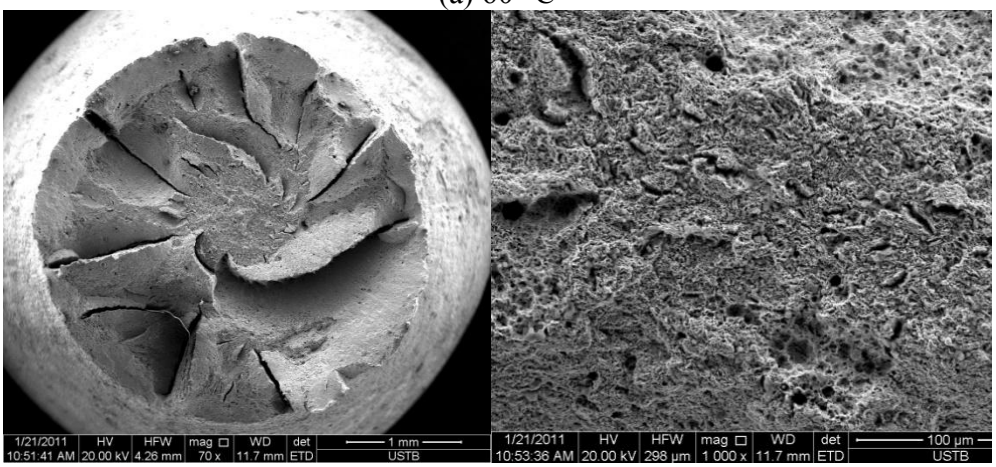

((b) 100 °C

Figure 10. SEM images of the fracture surfaces of the steel samples after SSRT.

The SCC mechanisms of TP95S in acidic solutions are predicted to be hydrogen-induced HIC or hydrogen embrittlement (HE) [22] and influenced by anodic dissolution. At temperatures lower than 80 °C, hydrogen in H2S easily penetrates into the steel as the temperature increases, which results in HIC or HE, particularly at temperatures between 20 °C and 50 °C. Moreover, hydrogen generated by the cathode reaction on the metal surface easily combines with molecules and rapidly overflows at temperatures higher than 80 °C. As such, SCC susceptibility is reduced because of the effects of HIC or HE. As the temperature further increases, the amount of hydrogen that entered into the steel rapidly decreases. At a electrochemical hydrogen charging temperature of 90 °C, the amount of hydrogen absorbed by TP95S steel during corrosion is reduced to one-tenth of the amount absorbed at 30 °C. This finding indicates that the SCC sensitivity of TP95S tube steel significantly decreases at 100 °C. Therefore, the generated hydrogen plays a significant role in the SCC of TP95S in the acidic gas field.

As shown in Fig. 7, the corrosion rate of steel increases in the presence of tensile stress. This finding implies that anodic dissolution plays an important role in the SCC of TP95S in the acidic gas field, especially during crack initiation, under which anodic dissolution caused by tensile stress may accelerate pitting and induce crack growth.

The SCC of TP95S tube steel in the acidic gas field is mixed controlled by anodic dissolution and HE [23, 24]. The decrease in pH and the increase in H2S density enhance the influence of HE [25, 26]. In particular, increased Cl− density plays an important role in anodic dissolution [27]. All of these factors enhance SCC susceptibility.

3.6. Mass loss

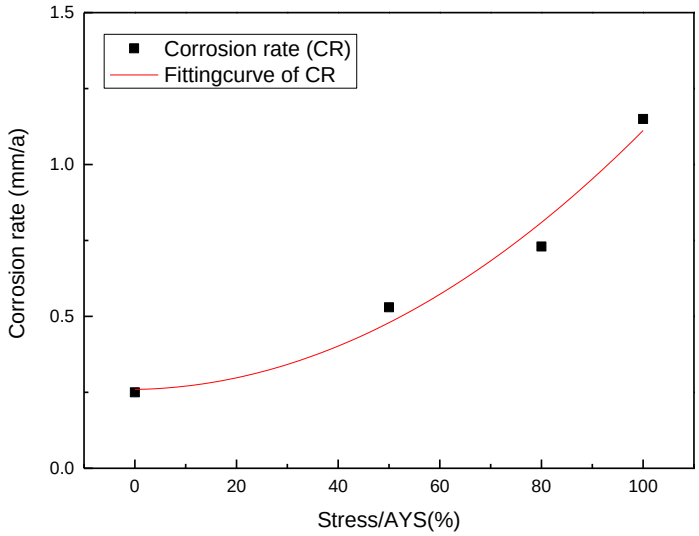

Figure 11. Corrosion rates of TP95S tube steel under different stress levels.

The average corrosion rate is calculated as follows:

$$\nu_W = \frac{W_{i0} - W_i}{A_i t} = \frac{\frac{R_{i0}^2 \bar{L}_i}{R_0^2 \bar{L}_0} W_0 - W_i}{2\pi R_{i0} \bar{L}_i t} \qquad (4)$$

where ν_W is the average corrosion rate, $g/(dm^2 \cdot a)$; W_0 is the weight of the standard sample in the gauge length, g; W_{i0} is the weight of the measured sample in the gauge length, g; W_i is the weight of the standard sample in the gauge length, g; A_i is the surface area of the measured sample in the gauge length, dm^2; t is the testing time, a (year); R_{i0} is the diameter of the tested sample in the gauge length, mm; R_0 is the diameter of the standard sample in the gauge length, mm; $\bar{L}_i$ is the gauge length of the measured sample, dm; and $\bar{L}_0$ is the gauge length of the standard sample, dm.

As samples are finely treated, $R_{i0} \approx R_0$; hence, equation 4 can be transformed into equation 5:

$$\nu_W = \frac{W_{i0} - W_i}{A_i t} = \frac{\frac{\bar{L}_i}{\bar{L}_0} W_0 - W_i}{2\pi R_{i0} \bar{L}_i t} \qquad (5)$$

When the average corrosion rate is characterized by depth, the corrosion rate is $\nu_d = \frac{\nu_w}{10\rho}$, where ν_d is the average corrosion rate, mm/a; and ρ is the density of the sample, g/mm^3.

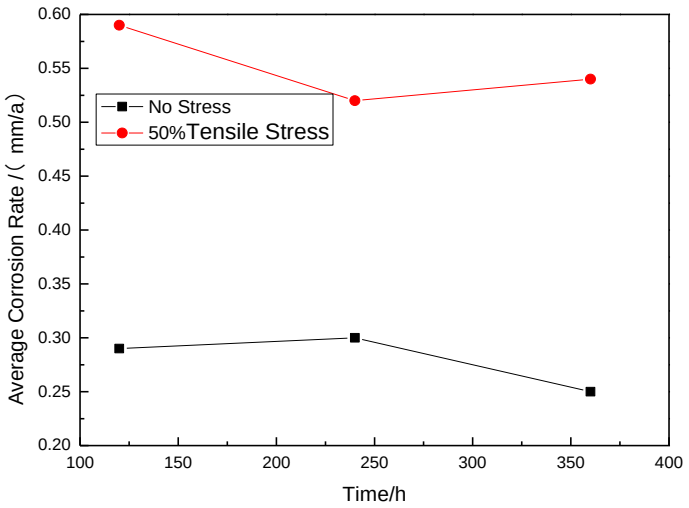

Figure 12. Average corrosion rates of TP95S tube steel under tensile stress or no stress.

Fig. 11 shows the influence of stress applied at different corrosion times on corrosion rate. The results indicate that stress state significantly affects corrosion rate. The existence of tensile stress accelerates corrosion rate; thus, anodic dissolution plays an important role in the stress corrosion of TP95S, especially during crack growth. Anodic dissolution caused by tensile stress may thus promote pitting growth and initiate cracking. The average corrosion rates of TP95S tube steel under tensile stress or no stress are shown in Fig. 12. The tests were performed for 120, 240, and 360 h. The results

indicate that the average corrosion rate of TP95S increases under tensile stress because the stress induces anodic dissolution, which may accelerate pitting and induce crack growth.

4. CONCLUSIONS

The SCC mechanism of TP95S steel in acidic gas fields is mixed controlled by AD and HE. The SCC susceptibility of TP95S is lower at 100 °C compared with that at 60 °C because of abated HE.

TP95S tube steel shows SCC susceptibility at tensile stresses higher than 70% of the yield strength. Thus, the stress level of TP95S tube steel during use should be kept lower than 70% and 50% of the yield strength at 100 °C and 60 °C, respectively. Furthermore, the applied tensile stress shortens the service life of TP95S tube steel in the acidic gas field.

ACKNOWLEDGEMENTS
Authors gratefully acknowledge financial support from National Basic Research Program of China (973 Program) (No. 2014CB643300), National Nature Science Foundation of China (No. 51131001 and 51471034) and Fundamental Research Funds for the Central Universities (No. FRF-TP-14-090A2).

References

1. S. Yahya, N. Othman, A. Daud, *Anti-Corrosion Methods and Materials*, 62(2015)301-306.
2. T. Liskiewicz, A. Al-Borno, A. Neville, Proceedings of the Corrosion Conference and Expo 2015. NACE International, 2015.
3. G. Genchev, K. Cox, T. Tran, *Corros. Sci*, 98(2015) 725-736.
4. M. Veloz, I. González, *Electrochimca Acta*, 48(2002)135–144.
5. T. das Chagas Almeida, E. Garcia, H. da Silva, *Int. J. Miner, Process*, 149(2016)25-33.
6. W. Zhao, Y. Zou, K. Matsuda, *Corros. Sci*, 102(2016) 455-468.
7. H. Rehan, S.Salih, H. El-Daley, A.Gad-Allah, *Collect. Czech. Chem. Commun*, 58 (1993) 547-554.
8. H. El-Lateef, *Corros. Sci*, 92(2015)104-117.
9. P. Bai, H. Zhao, S. Zheng, *Corros. Sci*, 93(2015) 109-119.
10. S. Tsai, H. Shih, *Corrosion Science*, 38 (1996)705-719.
11. F. Eliyan, E. Mahdi, A. Alfantazi, *Int. J. Electrochem. Sci*, 8(2013) 578-590.
12. N. Kairi, J. Kassim, *Int. J. Electrochem. Sci*, 8(2013)7138-7155.
13. N. Zadorozne, M. Giordano, A. Ares, Anodic Characteristics and Stress Corrosion Cracking Behavior of Nickel Rich Alloys in Bicarbonate and Buffer Solutions[J]. Corros. Sci, 2016.
14. L. Tsay, M. Chi, H. Chen, *Mater. Sci. Eng*., A 416(2006)155-160.
15. E. Sosa, I. García, R. Cabrera-Sierra, M.A. Rincón, M.T. Oropeza, *Electrochim. Acta* 47 (2002) 1197.
16. ASTM, Standard Practice for Calculation of Corrosion Rates and Related Information from Electrochemical Measurements, G102 – 89, 2004.
17. B. Mishra, S. Al-Hassan, D. Olson, *Corrosion*, 53(1997)852-859.
18. B.A. Bouckamp, Users Manual Equivalent Circuit, ver. 4.51, Faculty of Chem. Tech., Universidad of Twente, The Netherlands, 1993
19. V. Garcia-Arriaga, J. Alvarez-Ramirez, M. Amaya, *Corros. Sci*, 52(2010)2268-2279.

20. M. Zafar, R. Rihan, L. Al-Hadhrami, *Corros. Sci*, 94(2015) 275-287.
21. N. Perini, P. Corradini, V. Nascimento, *Corros. Sci*, 74(2013)214-222.
22. M. Kappes, M. Iannuzzi, R. Rebak, *Corros. Rev*, 33(2015) 99-99..
23. J. Tang, Y. Shao and J. Guo, *Corros. Sci*, 53(2011)1715-1723.
24. D. Li, L. Zhang, J. Yang, *International Journal of Minerals, Metallurgy and Materials*, 21(2014)388-394.
25. J. Tang, Y. Shao and J. Guo, *Corros. Sci*, 52(2010)2050-2058.
26. Y. Jianwei, Z. Lei and D. Ruiming, *J. Mater*,44(2008)1366-1371.
27. Y. Choi, J. Kim, *Corrosion*, 56(2000)1202-1210.